Origin of superconductivity in disordered tungsten thin films

Vivas Bagwe [*,†] Rishabh Duhan [*,‡] Bhagyashree Chalke, Jayesh Parmar,
Somak Basistha, and Pratap Raychaudhuri [§]
Tata Institute of Fundamental Research, Homi Bhabha Road, Colaba, Mumbai 400005, India

The most common allotrope of tungsten, α-W, has a superconducting transition at a temperature of ~ 11 mK. However, two other forms of tungsten have been reported to have superconducting transitions in the temperature range $T_c \sim 2-5$ K when synthesized as thin films: crystalline β-W and amorphous W (a-W). In this work we carry out a systematic study of W films synthesized using dc magnetron sputtering, using transport, low frequency magnetic shielding response, and transmission electron microscopy. Our results show that while a-W is indeed a conventional superconductor, β-W is not a superconductor down to 2.3 K. Superconductivity with $T_c > 3$ K in the putative β-W films probably originates from an amorphous phase that forms underneath the β-W phase. Our findings reconcile some of the anomalies earlier reported in β-W, such as the very small superconducting gap and the decrease of T_c with increase in film thickness.

I. INTRODUCTION

Bulk tungsten crystallizes in the body centered cubic α-W phase and has a very low superconducting transition temperature [1], $T_c \sim 11$ mK. However, tungsten thin films often show a much larger superconducting transition temperature [2,3] with $T_c \sim 2-5$ K. Early reports attributed this enhanced superconducting transition to the metastable β-W phase with A15 crystal structure [4,5]. β-W also has a large spin-orbit coupling [6], which along with superconductivity makes it a potential candidate for unconventional superconductivity [7] and spintronic applications [8,9]. At the same time, amorphous W (a-W) thin films with T_c as high as 5 K can also be grown by incorporating impurities during the deposition process. One way to obtain a-W films is by breaking down an organometallic precursor like W(CO)$_6$ using a focused ion beam [10–13], where the main impurities are carbon, oxygen, and gallium. Alternatively, a-W can also be synthesized using magnetron sputtering, by introducing nitrogen or oxygen gas along with argon during the deposition process [14–16]. While superconductivity in a-W appears to be robust, despite considerable work the origin of superconductivity in β-W films remains controversial. The situation is complicated by the fact that a small amount of impurity gas like nitrogen or oxygen during growth is required to stabilize the β-W phase and minimize the α-W impurity phase that inevitably forms along with the β-W phase [17–19]. Recent reports suggest that superconductivity in β-W is stabilized only in the presence of additional ingredients such as the formation of nanocrystalline structures [17] and disordered phases that grow alongside the β-W phase [15], or in the presence of a second impurity phase like WN$_x$ [14].

Early tunneling studies in β-W films using planar tunnel junctions revealed a large sample to sample variation in the superconducting energy gap (Δ), with gap to T_c ratio [3], $\frac{\Delta}{k_B T_c} \sim 1.1-1.8$ (where k_B is the Boltzmann constant). More recent optical conductivity measurements found the ratio to be [20] $\frac{\Delta}{k_B T_c} \sim 1$, which is much smaller than the expected value of 1.76 from Bardeen-Cooper-Schrieffer (BCS) theory. While such a small ratio could in-principle arise from isolated Fermi surface pockets that are much more weakly coupling than the rest of the Fermi surface, extrinsic effects such as a normal metal phase coexisting with the superconductor needs to be carefully ruled out. Furthermore, it has been reported that in β-W films, the superconducting transition temperature gets suppressed when the thickness is increased in the tens of nanometers range, which is in contrary to the behavior observed in most superconducting films [17]. This calls for a critical investigation on the origin of superconductivity in β-W thin films.

In this work, we investigate the origin of superconductivity in superconducting tungsten films grown through dc magnetron sputtering. Controlling the thickness and Ar/N$_2$ ratio during the deposition process, we can grow β-W and a-W films. We study the properties of both β-W and a-W films using a combination of structural, electrical, and magnetic measurements and low temperature scanning tunneling spectroscopy (STS). We observe that a-W behaves like a conventional BCS superconductor consistent with earlier reports [13]. In contrast superconductivity in the putative β-W films is highly anomalous: While bulk measurements show a clear superconducting transition, we do not observe a superconducting energy gap when the film is probed using STS. Cross-sectional TEM studies suggest that the superconductivity might not be associated with the β-W phase but with an amorphous W layer that forms underneath the β-W phase. The central result of this paper is that contrary to popular belief crystalline β-W might not be a superconductor down to 2.3 K.

---

*These authors contributed equally to this work.
†vivas@tifr.res.in
‡rishabh.duhan@tifr.res.in
§pratap@tifr.res.in

II. EXPERIMENTAL DETAILS

W films were grown from a 50.8 mm diameter W target using dc magnetron sputtering on oxidized Si, sapphire, and Nb-doped STO substrates at room temperature in Ar/N_2 gas mixture. Over the course of this study more than 100 films were deposited by varying the thickness and the Ar/N_2 gas ratio. In this work we will focus on films grown on 0.5 mm thick Si substrates with approximately 200 nm of thermal oxide on the top. The base pressure of the chamber prior to deposition was 8×10^{-7} mbar while the depositions were carried out at 10 mbar pressure. The composition of the gas mixture during growth was controlled with mass flow controllers. The flow rate of Ar was fixed at 27 SCCM (standard cubic centimeters per minute) whereas the N_2 flow rate was varied between 0 and 1 SCCM. The target substrate distance was fixed at 4.5 cm and the sputtering power was 60 W. The thickness of the films was measured using a stylus profilometer. Compositional analysis of several films was carried out using energy dispersive x-ray analysis (EDX).

For all films structural characterization was performed using x-ray diffraction (XRD). $\theta - 2\theta$ XRD scans were acquired keeping an offset of $4°$ with the plane of the film to avoid contribution from the substrate. Some films were also characterized using grazing incidence diffraction (GID) to get an insight of the structure at different thicknesses below the film surface. Transmission electron microscopy was performed using an aberration corrected (Cs corrected) FEI-Titan microscope operated at 300 kV and equipped with a field-emission gun source. To prepare the TEM specimen, the film was cut in 1.7 mm × 1 mm rectangular pieces using a diamond microsaw. A sandwich of two such samples was prepared using Gatan G1 epoxy and embedded in a Ti slot grid of dimensions 1.8 mm × 1 mm. The disk thus prepared was ground to an 80 micron thickness and then a dimple was made using a dimple grinder leaving a 10 micron thickness. This sample was then milled in a precision ion milling system using Ar ions. The sample was milled using top and bottom guns at 5 kV, $5°$ angle until perforation in the sample was observed; after that the sample was further polished with a low energy beam at 2 and 1 kV. The sample stage was cooled with liquid N_2 in order to avoid the sample getting altered due to local heating.

The superconducting transitions of the films were measured from their magnetic shielding response using a two-coil technique [21], in a continuous flow ^{4}He cryostat down to a lowest temperature of 2.3 K. In this technique, the film is sandwiched between a quadrupolar primary coil and a dipolar secondary coil [see inset of Fig. 2(a)] and the in-phase and out-of-phase component of the mutual inductance (M' and M'') is measured using a lock-in amplifier. The onset of superconductivity is marked by a rapid decrease in M' (and the appearance of a dissipation peak in M'') since the superconducting film partially shields the magnetic field generated in the primary coil from the secondary, thus providing a noncontact method for determining T_c. For some films, magnetotransport measurements were performed in a ^{3}He cryostat fitted with a 100 kOe superconducting solenoid. Electrical transport measurement was performed using the conventional four-probe method. Resistivity and Hall measurements were
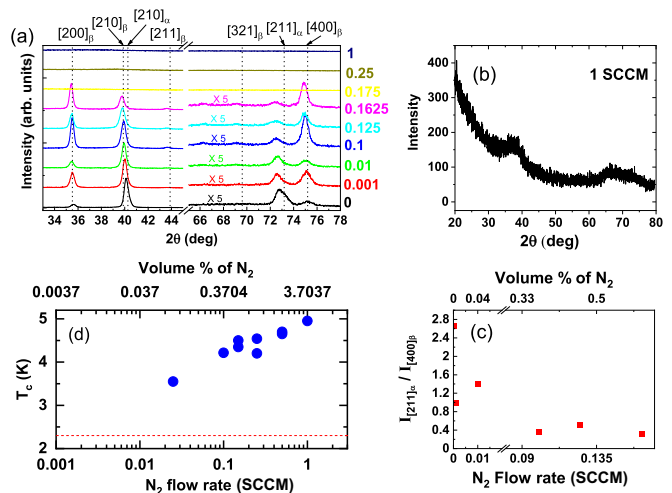
FIG. 1. (a) XRD $\theta - 2\theta$ scans for tungsten films grown in N_2/Ar atmosphere; the Ar flow rate was fixed at 27 SCCM whereas the N_2 flow rates for different films are shown in the right of the panel (in units of SCCM). Successive plots have been shifted upward for clarity. (b) XRD $\theta - 2\theta$ scan of the tungsten films grown with 1 SCCM flow rate of N_2. (c) Intensity ratio of $[211]_\alpha$ and $[400]_\beta$ peaks, $\frac{I_{[211]_\alpha}}{I_{[400]_\beta}}$, for films grown with different flow rates of N_2. (d) Variation of T_c for films grown in different N_2 flow rates. The red dashed line shows the lower temperature limit of our measurement. The top horizontal axes in panels (c), (d) show the volume percent of nitrogen in the Ar/N_2 gas mixture.

performed on samples deposited in a six-probe Hall bar geometry using a shadow mask. STS measurements were performed using a home-built scanning tunneling microscope [22] (STM) operating down to 410 mK and fitted with a 90 kOe superconducting solenoid. Since STS measurements require a pristine sample surface that is uncontaminated by exposure to air, we used the following protocol. After deposition, the sample is directly transferred from the deposition chamber using mechanical manipulators into an ultrahigh vacuum (UHV) suitcase kept at 10^{-9} mbar pressure using a room temperature getter pump and battery-operated ion pump. The UHV suitcase is then connected to the STM through a load-lock and the sample is transferred on the STM head using another set of mechanical manipulators without exposure to air.

III. RESULTS

Figure 1(a) shows representative $\theta - 2\theta$ scans for a set of W films grown with a different flow rate of N_2 during the deposition process. All films here have a thickness of 140 ± 10 nm. We observe the following general trend. For the films grown between 0 and 0.1625 SCCM we observe pronounced peaks close to $35.5°$ and $75.2°$ corresponding to $[200]_\beta$ and $[400]_\beta$ peaks, respectively. There is an additional peak at $72.6°$. This peak most likely corresponds to the $[211]_\alpha$ peak from a strained α-W impurity phase. While there are some peaks of W_2N_3 in this range, this is unlikely to be its origin for two reasons: First, we do not observe the more intense peaks corresponding to the same structure and, second, the peak
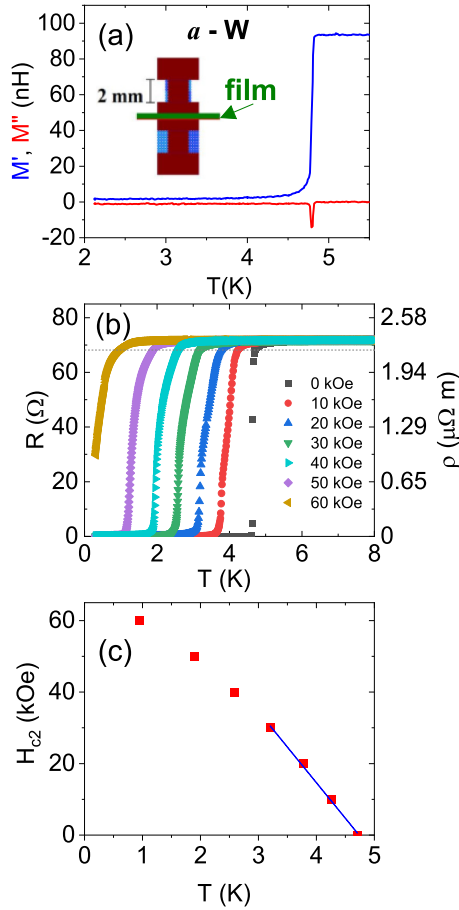
FIG. 2. (a) Magnetic shielding response of a 140 nm thick a-W film measured from the in-phase (M') and out-of-phase (M'') part of the mutual inductance. Inset: Schematics of the mutual inductance setup used to measure the magnetic shielding response of superconducting films. (b) Resistance/resistivity versus temperature of an a-W film in different magnetic fields. The dashed horizontal line shows 95% of the normal state resistance from which H_{c2} is determined. (c) Temperature variation of H_{c2} for the same film; the solid blue line shows the linear variation of H_{c2} close to T_c.

intensity does not increase with N_2 flow rate. Furthermore, in all the crystalline films we observe a pronounced peak close to 40°. For the sample grown in pure Ar atmosphere, this peak is between the expected values for $[110]_\alpha$ (at 40.26°) and $[210]_\beta$ (at 39.88°). This could in principle be a strained $[110]_\alpha$ peak. However, since all the peaks here are broad due to the disordered nature of these films, it is more likely to have contribution from both $[110]_\alpha$ and $[210]_\beta$. As the N_2 flow rate is increased from 0 to 0.1625 SCCM we observe that this peak shifts toward the expected value of the β-W phase showing a gradual stabilization of the β-W phase. The same can be seen from the intensity ratio of $[211]_\alpha$ and $[400]_\beta$ peaks which decreases from $\frac{I_{[211]_\alpha}}{I_{[400]_\beta}} \sim 2.65$ to $\frac{I_{[211]_\alpha}}{I_{[400]_\beta}} \sim 0.2$ in the same range [Fig. 1(c)]. One point to note is that a small amount of β phase is present even when the growth is performed without N_2, in contrast to some earlier studies [15,19]. This is due to the slightly higher base pressure in our chamber, where residual impurity gas can cause a partial conversion to the β phase even when no N_2 is intentionally introduced. However,

with further increase of N_2 in the sputtering gas the film gets completely amorphized. Films grown with N_2 flow rate between 0.25 and 1 SCCM always show very broad humps close to 35° and 65° and no crystalline peak [Fig. 1(b)] consistent with the formation of a-W . Between 0.1 and 0.25 SCCM, we observed that the structure of the films is extremely sensitive to deposition conditions. In this window, sometimes the same N_2 flow rate resulted in films that show prominent β-W peaks, very weak β-W peaks riding over a large amorphous background, or that are completely amorphized, especially when the films were grown several days apart. EDX compositional analysis of several a-W films grown in 1 SCCM N_2 flow-rate showed the presence of 3–4 at. % of nitrogen. It is therefore likely that a-W films contain some amorphous phases of tungsten nitrides (e.g., $WN_{0.2}$, $WN_{0.6}$) in addition to amorphous W as shown in earlier photoemission studies [15]. Figure 1(d) shows the variation of T_c with N_2 flow rate. Films grown with a N_2 flow of 0.01 SCCM or lower did not show any superconducting transition down to 2.3 K. We observe the onset of superconductivity above a 0.025 SCCM N_2 flow rate. However, some films grown below a 0.1 SCCM N_2 flow rate did not show superconductivity down to 2.3 K. Superconductivity was consistently observed above 0.1 SCCM and films grown with N_2 flow rates larger than 0.25 SCCM consistently showed superconductivity with $T_c > 4$ K and typical T_c variation less than 10%. We will discuss this in more detail below.

Of the films deposited, we obtained superconductivity most consistently in the a-W films with the superconducting transition varying in the range $T_c \sim 4.4 - 5.2$ K. Figure 2(a) shows the representative magnetic shielding response of one a-W film (140 nm thickness) with $T_c \sim 4.8$ K. The single sharp drop in M' at T_c and the clean dissipative peak in M'' are both signatures of clean homogeneous film. Figure 2(b) show the resistance (R) versus temperature (T) at various magnetic fields. From the R-T we extract in Fig. 2(c) the temperature variation of the upper critical field, H_{c2}, defined as the point where the resistance reaches 95% of the normal state value. Close to T_c, H_{c2} varies linearly with temperature following a relation $H_{c2}(T) \sim (T - T_c)$, as expected from Ginzburg-Landau theory. From this linear slope we extract $H_{c2}(0) \sim 65$ kOe using the Werthamer-Helfand-Hohenberg [23] (WHH) relation, $H_{c2}(0) = -0.693 T_c \frac{dH_{c2}}{dT}|_{T \approx T_c}$. The measured value of H_{c2} at 1 K is 60 kOe, consistent with this estimate. To further understand the superconducting state, we investigated a similar sample using STM. Figure 3(a) shows the topography of the sample. The root mean square surface roughness is ~ 0.7 nm. Figure 3(b) shows the normalized differential conductance [$G_N(V) = \frac{dI}{dV}|_V / \frac{dI}{dV}|_{4 \text{ mV}}$] as a function of voltage at different temperatures, averaged over a uniformly placed 8×8 grid over this area. The $G_N(V) - V$ curves display symmetric coherence peaks and minima at low bias consistent with what is expected for a conventional superconductor. We fit each curve with the standard tunneling equation [24], using the broadened Bardeen-Cooper-Schrieffer (BCS) density of states: $N(E) = \text{Re}\{\frac{|E+i\Gamma|}{\sqrt{(E+i\Gamma)^2 - \Delta^2}}\}$, where Δ is the superconducting energy gap and Γ is a parameter that accounts for nonthermal sources of broadening. While originally introduced as a phenomenological parameter [25], it has been recently shown that this parameter can microscopically
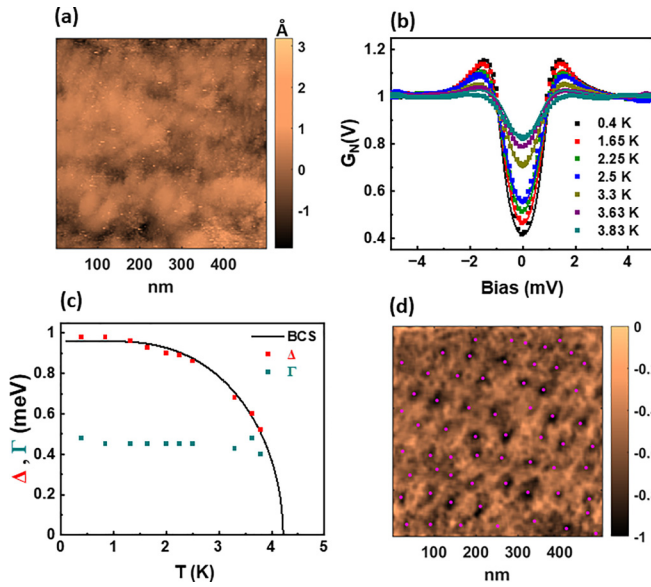
FIG. 3. (a) Topographic map over 500 nm × 500 nm area for a 140 nm thick *a*-W thin film measured using STM at 4 K; the bias voltage is 15 mV and tunneling current is 150 pA. (b) Normalized conductance $G_N(V)$ as a function of bias voltage at different temperatures in zero magnetic field, averaged over 64 equally spaced points over this area; the conductance is normalized at 4 mV. The solid lines show the fits to the spectra. (c) Temperature variation of the superconducting energy gap Δ and broadening parameter Γ extracted from the fits; the solid line is the expected BCS variation of Δ. (d) Normalized $\frac{dI}{dV}\big|_{V=1.5\ \text{mV}}$ map over the same area at 410 mK in a magnetic field of 5 kOe; the color scale is offset subtracted and normalized such that −1 and 0 correspond to the minimum and maximum conductance values, respectively. The vortices appear at local minima in the conductance map and are shown as purple points.

originate from disorder scattering [26]. We extract, $\Delta(0) \sim$ 1 meV, which corresponds to $\frac{\Delta(0)}{k_B T_C} \sim 2.6$. This is larger than the weak coupling BCS value and similar to strong coupling superconductors [27] like Hg. The temperature variation of Δ [Fig. 3(c)] follows the expected BCS variation within experimental accuracy. On the other hand, $\Gamma \sim 0.48$ meV is relatively large and temperature independent. Such a large temperature independent value of Γ is typical of amorphous superconductors [28,29] and reflects the strong disorder scattering in these materials [26]. Figure 3(d) shows the conductance map acquired at a bias voltage of $V = 1.5$ mV close to the coherence peak ($\frac{dI}{dV}\big|_{V=1.5\ \text{mV}}$), over the same area at 0.41 K with a magnetic field of 5 kOe applied perpendicular to the film plane. In the conductance map each vortex appears as a dark spot, corresponding to a local conductance minimum [30,31]. This identification was further confirmed by counting the number of vortices. Dividing the total magnetic flux by the flux quantum $\Phi_0 = \frac{h}{2e}$ we expect to see 61 vortices within the field of view, which is very close to the observed value of 62 vortices.

Superconductivity in β-W films was much less consistent than in amorphous films. Due to the difficulty in obtaining films with the same structural characteristic in the growth window where the β-W phase is most stable, we synthesized many films with N_2 flow rates between 0.001 and 0.2
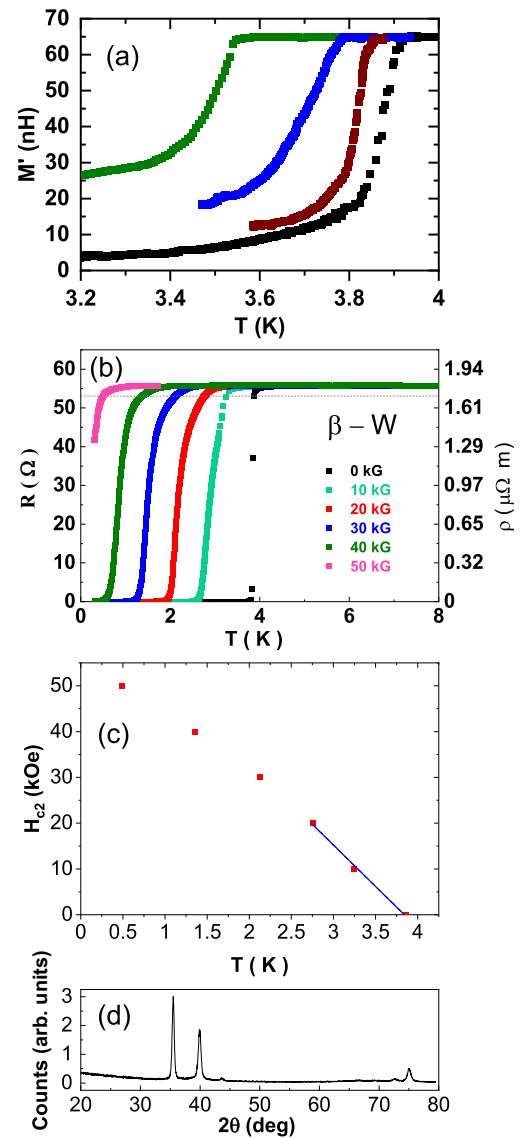
FIG. 4. (a) Magnetic shielding response of four β-W films showing superconducting transition between 3 and 4 K. (b) Resistance/resistivity versus temperature of one β-W film with $T_c \sim$ 3.85 K in different magnetic fields. The dashed horizontal line shows 95% of the normal state resistance from which H_{c2} is determined. (c) Temperature variation of H_{c2} for the same film; the solid blue line shows the linear variation of H_{c2} close to T_c. (d) XRD $\theta - 2\theta$ scan of the same film showing the diffraction peaks corresponding to β-W.

SCCM over several months. As expected, some of the films synthesized toward the upper end of this window turned out to be completely amorphous. Of the 22 samples that showed clear β-W peaks, eight showed a superconducting transition down to 2.3 K. The magnetic screening responses for four films with $T_c > 3$ K are shown in Fig. 4(a). However, the T_c's of β-W films were consistently lower than 4 K. From XRD we observed that all samples had a small amount of α-W impurity. One sample with $T_c \sim 3.85$ K was chosen for detailed transport measurements. Figure 4(b) shows the R-T of this sample in different magnetic fields. The zero-field transition is sharp and H_{c2} [Fig. 4(c)] measured using the same criterion as before is of the same order of magnitude
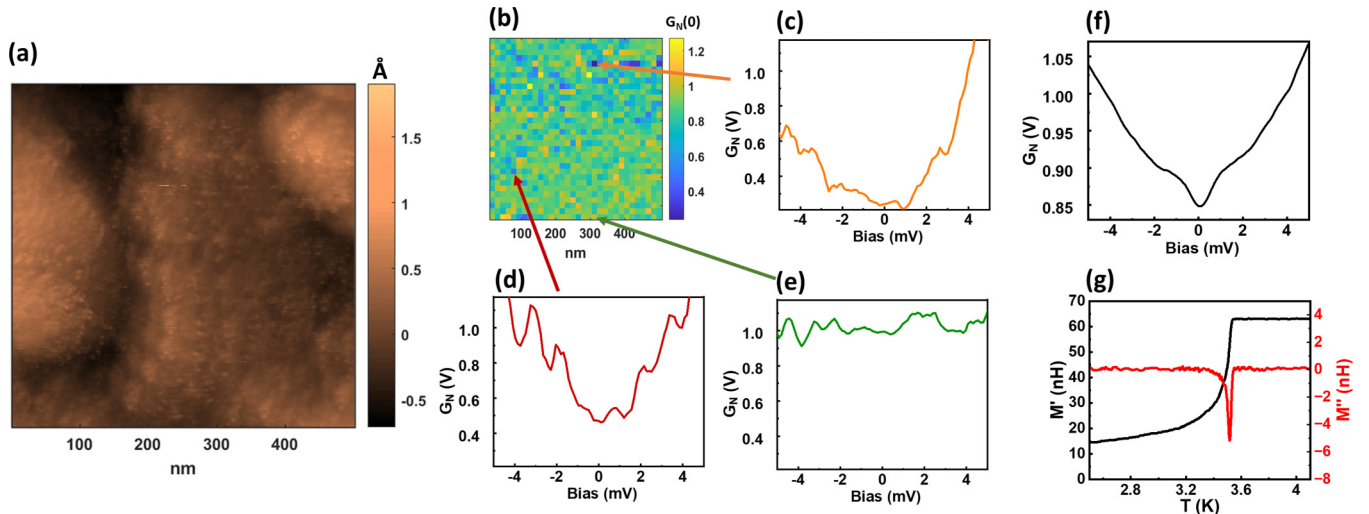
FIG. 5. (a) Topographic map over 500 nm $\times$ 500 nm area for a 140 nm thick β-W thin film measured using STM at 4 K; the bias voltage is 15 mV and tunneling current is 150 pA. (b) Normalized zero bias conductance [$G_N(0) = \frac{\frac{dI}{dV}\big|_{V=0}}{\frac{dI}{dV}\big|_{V=4 \text{ mV}}}$] map over the same area. (c–e) Representative $G_N(V)$ versus V spectra at three different locations. (f) Average normalized conductance $G_N(V)$ versus V spectra over the entire area; a small suppression in conductance is observed below 1 mV riding over the overall V shape extending to high bias. (g) Magnetic shielding response for the same film measured from the in-phase (M') and out-of-phase (M'') part of the mutual inductance.

as a-W . From the linear slope of H_{c2} versus T close to T_c, we estimate $H_{c2}(0) \approx 48$ kOe. This value is slightly exceeded at 0.5 K where $H_{c2} \sim 50$ kOe. It is difficult to ascribe physical significance to this small discrepancy since the value of H_{c2} can change by a few percent based on the precise criterion used. The normal state resistivity is about 20% lower than the amorphous film of the same thickness. The XRD for this film [Fig. 4(d)] shows clear peaks corresponding to the β-W phase and a small contribution from the α-W impurity.

Since β-W films did not consistently show superconductivity, we performed STS measurements on several samples adopting the following protocol: We first performed STS measurement on an uncontaminated surface without exposing to air; after completing STS measurements the sample was taken out and the T_c was determined through magnetic shielding response measurements. While some of the samples showed a superconducting transition in the magnetic shielding response, none of the samples showed a clear signature of superconductivity in STS measurements. Figure 5(a) shows the topography of a β-W film with $T_c \sim 3.55$ K. $G(V)$-V curves were acquired over this area on a 32×32 grid at 410 mK in zero magnetic field. Figure 5(b) shows the normalized zero bias conductance map over this area. The individual spectra either showed a broad V shape [Figs. 5(c)–5(e)] extending up to high bias, or were nearly flat, and none of them showed any clear signature of superconductivity related features. However, a weak signature of superconductivity below 1 mV was observed when we inspected the average of all 1024 spectra [Fig. 5(f)]. Here in addition to the broad V shape a small additional decrease in conductance ($\sim$5%) becomes visible below 1 mV. This weak low bias feature is reminiscent of proximity induced superconductivity that is observed when a superconductor is covered with a normal metal [32]. Figure 5(g) shows the magnetic shielding response measured on the same film. The shielding response shows a drop in M' at the superconducting transition and the associated dissipative peak in M.

To understand the anomalous behavior of β-W films, we carried out detailed cross-sectional TEM (csTEM) measurements on the same sample. Figures 6(a) and 6(b) show the csTEM images acquired at the top and bottom (close to the substrate) of the film along with the selective area electron diffraction (SAED) pattern from the top and the bottom [Figs. 6(c) and 6(d)] taken with a 5 μm aperture. Figures 6(e) and 6(f) show the magnified view of the areas in the 10 nm $\times$ 10 nm white box in Figs. 6(a) and 6(b), respectively. We observe that the structure of the film is not the same at the top and the bottom. At the top of the film, we can clearly see crystalline structure in the image. The SAED pattern [Fig. 6(c)] contains a large number of sharp spots forming a ring pattern which is expected when the diffraction is from several crystallites within the field view. In Fig. 6(g) we show the two-dimensional Fourier transform (2DFT) of the area shown in Fig. 6(e); Fig. 6(g) shows sharp spots that we can index with the β-W crystal structure. In contrast, no crystalline structure is discernible close to the substrate; here both the SAED [Fig. 6(d)] and the 2DFT of the area shown in Fig. 6(f) [Fig. 6(h)] show diffuse rings corresponding to either a nanocrystalline or an amorphous state.

To understand the evolution of the structure more carefully, we recorded nanobeam diffraction (NBD) patterns with an electron beam spot size of 1.5 nm [Fig. 7(b)], at 23 locations across the cross section of a 220 nm thick film, where location 1 is close to the top of the film and location 23 is close to the substrate [Fig. 7(a)]. The panels labeled 1–23 show representative NBD patterns at 14 locations. The NBD pattern at location 1 shows sharp Bragg spots corresponding to a crystalline structure. These Bragg spots are visible until location 4 which is about 29 nm from the film surface. Beyond this the NBD pattern displays only a ring that progressively becomes diffuse as we go toward the substrate. This implies either the presence of nanocrystallites or an amorphous structure with short-range correlations. Beyond location 15 (corresponding
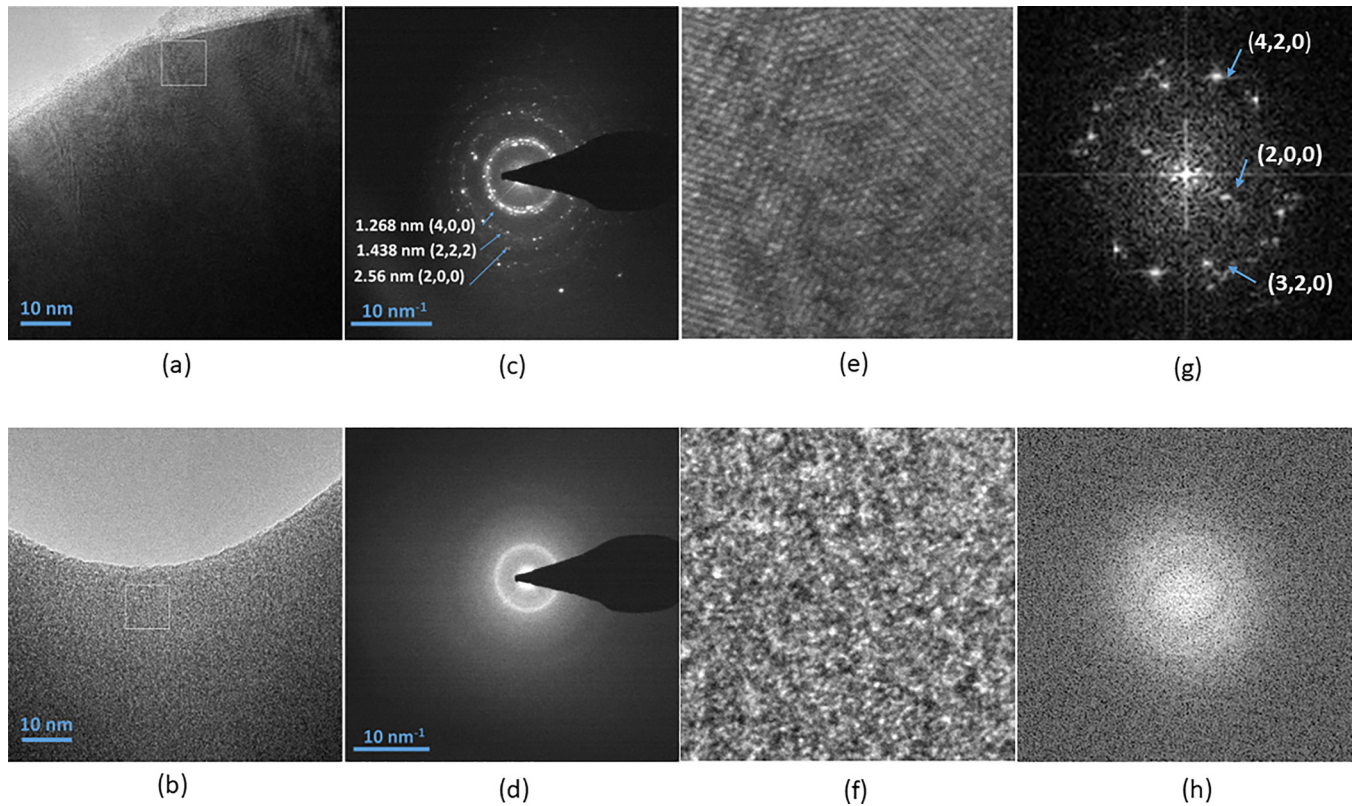
FIG. 6. (a), (b) Transmission electron micrograph of the top (a) and bottom (b) of a 220 nm thick β-W thin film. (c), (d) SAED pattern from the top (c) and bottom (d) of the film. (e), (f) Expanded view of the 10 nm $\times$ 10 nm area within the white box in (a), (b), respectively. (g), (h) 2DFT of images (e), (f), respectively; some Bragg spots in (g) are indexed with the β-W structure.

to 133 nm from the film surface), the ring also disappears, and we see only a diffuse intensity corresponding to a completely amorphous structure. These results strongly suggest the existence of approximately 90 nm thick amorphous W beneath the β-W film. In contrast, similar measurements performed on

a-W film do not show any structural variation within the film thickness and show an amorphous structure everywhere.

Since the β-W structure appears to form over a critical thickness of an amorphous W layer, one could expect very thin films to be purely a-W. To check this hypothesis, we deposited
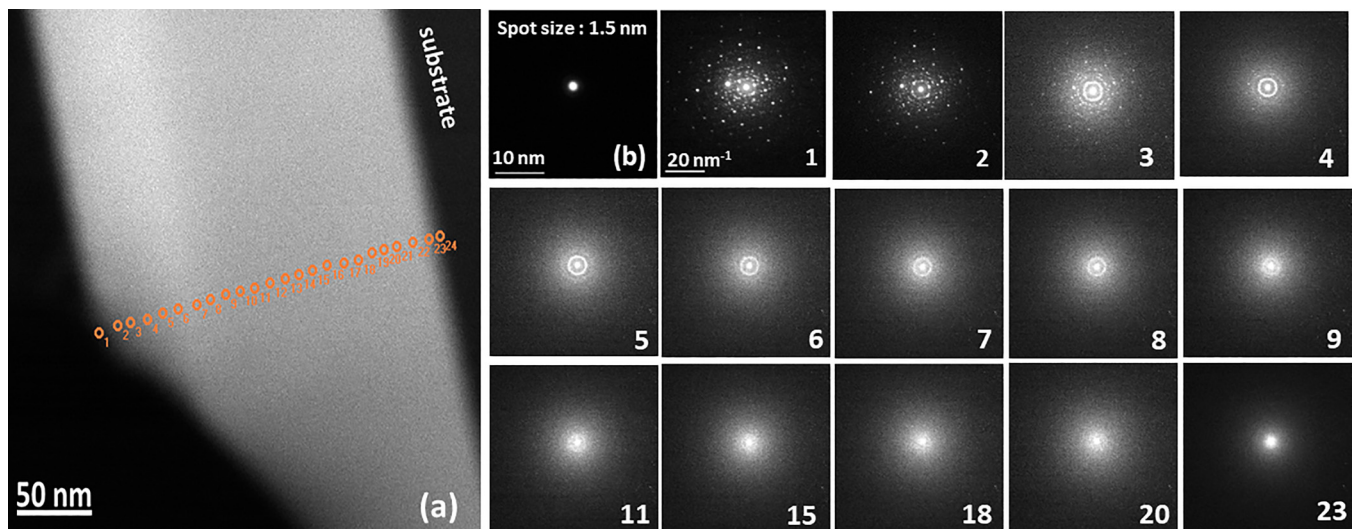
FIG. 7. (a) Cross-sectional view of a β-W film. The point marked 1 is at the top of the film, while 23 is at the bottom. (b) Image of the 1.5 nm nanobeam used for the NBD acquired at locations 1–23. The panels marked 1–23 show the NBD patterns at the location marked by the same number in panel (a). We observe a gradual change from crystalline to amorphous structure as one goes from the top to the bottom of the film.
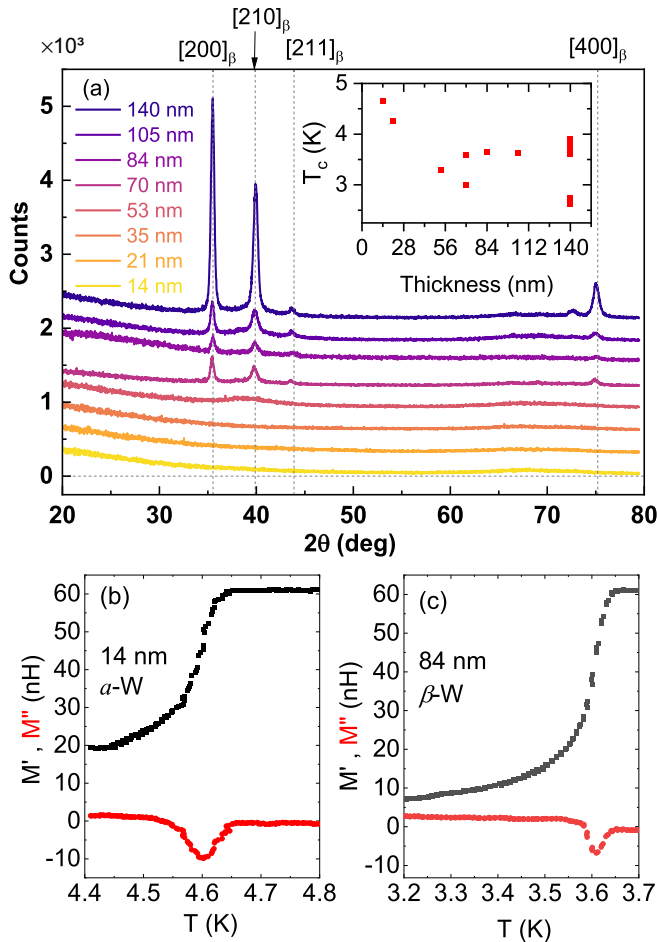
FIG. 8. (a) XRD $\theta - 2\theta$ scans of tungsten films of different thicknesses grown in 0.16 SCCM N_2 and 27 SCCM Ar flow. Films with thickness up to 53 nm are amorphous. Peaks corresponding to β-W start gradually appearing for films with thickness larger than 70 nm and become more intense with increase in thickness. Each successive graph has been shifted upward for clarity. Inset: Variation of T_c with film thickness grown under same deposition conditions; for some thicknesses we have shown T_c for multiple films of the same thickness to give an idea of sample to sample variation, which becomes more pronounced in the thickness range in which we observe β-W crystalline peaks. (b), (c) Representative magnetic shielding response measured from the in-phase (M') and out-of-phase (M'') part of the mutual inductance is shown for the 14 and 84 nm thick films, respectively.

a series of films with different thicknesses at 0.16 SCCM N_2 flow, in a set of consecutive runs starting from the thinnest sample. Figure 8(a) shows the XRD $\theta - 2\theta$ scans for this set of films. Indeed, up to a thickness of 35 nm we do not observe any Bragg peak showing the formation of pure a-W films. For the film with 53 nm thickness broad humps start appearing around the positions where Bragg peaks are expected for the β-W structure, indicating the formation of nanocrystals. Clear Bragg peaks corresponding to β-W appear at 70 nm thickness. Between 70 and 140 nm the Bragg peaks get more intense. For the 140 nm thick film we can identify the $[211]_\alpha$ peak showing the presence of α-W impurity, consistent with our earlier discussion on films with similar thickness. The inset

of Fig. 8(a) shows the variation of T_c for films of different thickness deposited under the same conditions. Films grown with thickness in the range where we observe pure a-W films have $T_c > 4$ K. In contrast, in the range of thickness where we can identify the formation of the β-W phase, T_c drops to lower than 3.8 K. The magnetic shielding responses of two representative films are shown in Figs. 8(b) and 8(c).

IV. DISCUSSION

We can now put these results in perspective. We have consistently observed superconductivity only in a-W films grown in the presence of moderate N_2 impurities during growth. Since we cannot identify any crystalline WN_x phase, we conclude that the N_2 either gets incorporated as interstitial atoms or forms amorphous phases of WN_x as suggested in some earlier studies [15]. In contrast, the origin of superconductivity in films that show pronounced β-W peaks in XRD is more complex. First, the superconducting transition temperatures of these films vary widely, and many films turn out to be nonsuperconducting down to 2.3 K. Those which exhibited superconductivity had a transition temperature <4 K, which is smaller than a-W films. However, even for films that showed a superconducting transition from transport and magnetic measurements, we observed only a very weak signature of proximity induced superconductivity at the surface of the film using STM. Combining the information obtained from structural measurements, we conclude that superconductivity originates from the amorphous tungsten underlayer, whereas β-W itself remains nonsuperconducting. In the presence of sharp diffraction peaks from β-W, it is easy to miss the presence of the amorphous layer from XRD measurements. We note that if superconductivity arises from the amorphous underlayer, the normal β-W film above will influence superconductivity in two different ways. First, weak superconductivity will get induced through the proximity effect in the intrinsically normal metal β-W thus explaining the proximity induced minigap [32] in our experiments. On the other hand, the T_c of the amorphous superconducting underlayer would also get partially suppressed due to the inverse proximity effect, explaining why films showing the β-W phase always show T_c that is smaller than pure a-W films. This observation is consistent with an earlier report where a 60 nm thick β-W film was seen to have lower T_c compared to a 35 nm film [17]. It is pertinent to note that in Ref. [17], the 35 nm film only showed a very broad peak in XRD suggesting an amorphous structure as opposed to the sharp diffraction peaks observed in the 60 nm film, which is again consistent with our results.

One puzzling aspect of this study is the large sample to sample variation in T_c of β-W films sometimes grown under the same conditions. The most likely reason for this is that the pure β-W phase is stable in a narrow window of N_2 flow rate, which is sensitive to small changes in other deposition parameters. As a result, small changes in parameters such as target substrate distance and sputtering power, as well as microscopic details of the substrate, can all change the phase boundaries between α-W $\rightarrow$ β-W $\rightarrow$ a-W, making it difficult to control the thickness of the superconducting amorphous underlayer. However, this issue will need to be investigated further.

Finally, we would also like to comment on the optical conductivity measurements [20] that reveal an anomalously small superconducting energy gap in β-W . While a gap ratio, $\frac{\Delta}{k_B T_c}$, larger than the expected BCS value of 1.76 is often observed in strongly coupling superconductors [33], a ratio that is smaller than the BCS ratio is rare. In light of our results, we believe that the small gap is related to the superconducting/nonsuperconducting sandwich structure in β-W films. We note that unlike STM which probes the sample's surface, THz optical conductivity performed in the transmission geometry probes the entire depth of the film which will give an average response from both the superconducting amorphous and nonsuperconducting β-W layers. This would naturally explain the smaller than expected depletion of the real part of the conductivity below T_c and a small Δ, something that should be quantitatively verified from detailed calculations.

V. CONCLUSION

In this paper, we revisited the decades-old problem on the origin of superconductivity in tungsten thin films. Our results show that a-W is a conventional strong coupling superconductor. On the other hand, contrary to common belief, crystalline β-W might not be a superconductor down to 2.3 K. The superconducting transition in β-W films with $T_c \sim 3-4$ K

originates from an amorphous tungsten underlayer that forms below the β-W phase. A similar conclusion was recently arrived at in Ref. [15] which focused primarily on x-ray photoemission measurements. In a very recent paper [19], it has been suggested that pure β-W could be a superconductor with a lower $T_c \sim 1.1$ K. Nevertheless, the nonintrinsic nature of superconductivity observed in β-W films with much higher T_c provides a plausible explanation of several unusual superconducting properties reported in this material and should be carefully considered in any future study of this material.

[1] J. W. Gibson and R. A. Hein, Superconductivity of tungsten, Phys. Rev. Lett. **12**, 688 (1964).

[2] O. F. Kammerer and M. Strongin, Superconductivity in tungsten films, Phys. Lett. **17**, 224 (1965).

[3] S. Basavaiah and S. R. Pollack, Superconductivity in β-tungsten films, J. Appl. Phys. **39**, 5548 (1968).

[4] W. L. Bond, A. S. Cooper, K. Andres, G. W. Hull, T. H. Geballe, and B. T. Matthias, Superconductivity in films of β tungsten and other transition metals, Phys. Rev. Lett. **15**, 260 (1965).

[5] S. M. Rossnagel, I. C. Noyan, and C. Cabral, Jr., Phase transformation of thin sputter-deposited tungsten films at room temperature, J. Vac. Sci. Technol. B **20**, 2047 (2002).

[6] C.-F. Pai, L. Liu, Y. Li, H. W. Tseng, D. C. Ralph, and R. A. Buhrman, Spin transfer torque devices utilizing the giant spin Hall effect of tungsten, Appl. Phys. Lett. **101**, 122404 (2012).

[7] J. Li, S. Ullah, R. Li, M. Liu, H. Cao, D. Li, Y. Li, and X.-Q. Chen, Topological massive Dirac fermions in β-tungsten, Phys. Rev. B **99**, 165110 (2019).

[8] S. Mondal, S. Choudhury, N. Jha, A. Ganguly, J. Sinha, and A. Barman, All-optical detection of the spin Hall angle in W/CoFeB/SiO$_2$ heterostructures with varying thickness of the tungsten layer, Phys. Rev. B **96**, 054414 (2017).

[9] K.-U. Demasius, T. Phung, W. Zhang, B. P. Hughes, S.-H. Yang, A. Kellock, W. Han, A. Pushp, and S. S. P. Parkin, Enhanced spin–orbit torques by oxygen incorporation in tungsten films, Nat. Commun. **7**, 10644 (2016).

[10] E. S. Sadki, S. Ooi, and K. Hirata, Focused-ion-beam-induced deposition of superconducting nanowires, Appl. Phys. Lett. **85**, 6206 (2004).

[11] W. Li, J. C. Fenton, Y. Wang, D. W. McComb, and P. A. Warburton, Tunability of the superconductivity of tungsten films grown by focused-ion-beam direct writing, J. Appl. Phys. **104**, 093913 (2008).

[12] Y. Sun, J. Wang, W. Zhao, M. Tian, M. Singh, and M. H. W. Chan, Voltage-current properties of superconducting amorphous tungsten nanostrips, Sci. Rep. **3**, 2307 (2013).

[13] I. Guillamón, H. Suderow, S. Vieira, A. Fernández-Pacheco, J. Sesé, R. Córdoba, J. M. De Teresa, and M. R. Ibarra, Nanoscale superconducting properties of amorphous W-based deposits grown with a focused-ion-beam, New J. Phys. **10**, 093005 (2008).

[14] J. A. Hofer and N. Haberkorn, Superconductivity in nanocrystalline tungsten thin films growth by sputtering in a nitrogen-argon mixture, Thin Solid Films **685**, 117 (2019).

[15] J. A. Hofer, S. Bengio, S. Suarez, and N. Haberkorn, Elucidating the role of disorder introduced by nitrogen in the superconducting properties of tungsten thin films, Mater. Adv. **4**, 150 (2023).

[16] N. Radic, A. Tonejc, J. Ivkov, P. Dubcek, S. Bernstorff, and Z. Medunic, Sputter-deposited amorphous-like tungsten, Surf. Coat. Technol. **180**, 66 (2004).

[17] A. Chattaraj, M. M. Patidar, V. Ganesan, S. Joulie, V. Serin, A. Claverie, V. Kumar, and A. Kanjilal, Atomic scale microstructural insights of superconducting β-tungsten thin films, J. Mater. Res. **37**, 4338 (2022).

[18] Y. G. Shen and Y. W. Mai, Influences of oxygen on the formation and stability of A15 β-W thin films, Mater. Sci. Eng. A **284**, 176 (2000).

[19] J. A. Hofer, P. Pedrazzini, S. Bengio, and N. Haberkorn, Superconductivity in low nitrogen concentration stabilized β-tungsten thin films, Mater. Lett. **360**, 136007 (2024).

[20] P. Chauhan, R. Budhani, and N. P. Armitage, Anomalously small superconducting gap in a strong spin-orbit coupled

superconductor: β-tungsten, Phys. Rev. B **105**, L060503 (2022).

[21] S. Kumar, C. Kumar, J. Jesudasan, V. Bagwe, P. Raychaudhuri, and S. Bose, A two-coil mutual inductance technique to study matching effect in disordered NbN thin films, Appl. Phys. Lett. **103**, 262601 (2013).

[22] A. Kamlapure, G. Saraswat, S. C. Ganguli, V. Bagwe, P. Raychaudhuri, and S. P. Pai, A 350 mK, 9 T scanning tunneling microscope for the study of superconducting thin films on insulating substrates and single crystals, Rev. Sci. Instrum. **84**, 123905 (2013).

[23] N. R. Werthamer, E. Helfland, and P. C. Honenberg, Temperature and purity dependence of the superconducting critical field, H_{c2}. III. Electron spin and spin-orbit effects, Phys. Rev. **147**, 295 (1966).

[24] M. Tinkham, *Introduction to Superconductivity* (McGraw-Hill, New York, 1996).

[25] R. C. Dynes, V. Narayanamurti, and J. P. Garno, Direct measurement of quasiparticle-lifetime broadening in a strong-coupled superconductor, Phys. Rev. Lett. **41**, 1509 (1978).

[26] F. Herman and R. Hlubina, Microscopic interpretation of the Dynes formula for the tunneling density of states, Phys. Rev. B **94**, 144508 (2016).

[27] S. Bermon and D. M. Ginsberg, Electron tunneling into superconducting mercury films, Phys. Rev. **135**, A306 (1964).

[28] S. Dutta, J. Jesudasan, and P. Raychaudhuri, Magnetic field induced transition from a vortex liquid to Bose metal in ultrathin a-MoGe thin film, Phys. Rev. B **105**, L140503 (2022).

[29] R. Duhan, S. Sengupta, R. Tomar, S. Basistha, V. Bagwe, C. Dasgupta, and P. Raychaudhuri, Structure and dynamics of a pinned vortex liquid in a superconducting $a-Re_6Zr$ thin film, Phys. Rev. B **108**, L180503 (2023).

[30] S. C. Ganguli, H. Singh, G. Saraswat, R. Ganguly, V. Bagwe, P. Shirage, A. Thamizhavel, and P. Raychaudhuri, Disordering of the vortex lattice through successive destruction of positional and orientational order in a weakly pinned $Co_{0.0075}NbSe_2$ single crystal, Sci. Rep. **5**, 10613 (2015).

[31] I. Roy, S. Dutta, A. N. R. Choudhury, S. Basistha, I. Maccari, S. Mandal, J. Jesudasan, V. Bagwe, C. Castellani, L. Benfatto, and P. Raychaudhuri, Melting of the vortex lattice through intermediate hexatic fluid in an a-MoGe thin film, Phys. Rev. Lett. **122**, 047001 (2019).

[32] A. K. Gupta, L. Crétinon, N. Moussy, B. Pannetier, and H. Courtois, Anomalous density of states in a metallic film in proximity with a superconductor, Phys. Rev. B **69**, 104514 (2004).

[33] D. Rainer and J. A. Sauls, *Strong Coupling Theory of Superconductivity, Superconductivity: From Basic Physics to New Developments*, edited by P. N. Butcher and Y. Lu (World Scientific, Singapore, 1995), pp. 45–78.